2021 IEEE Applied Power Electronics Conference and Exposition (APEC) | 978-1-7281-8949-9/21/$31.00 ©2021 IEEE | DOI: 10.1109/APEC42165.2021.9487239

Modeling and Design of a 6-Phase Ultra-High-Speed Machine for ELF/VLF Wireless Communication Transmitter

Md Khurshedul Islam
Electrical and Computer Engineering
Mississippi State University
mi264@msstate.edu

Seundeog Choi
Electrical and Computer Engineering
Mississippi State University
seungdeog@ece.msstate.edu

***Abstract*— This paper presents the modeling, design, and Multiphysics analysis of a 2000-W, 500000-rpm ultra-high-speed (UHS) machine for a mechanical-based antenna (AMEBA) application. The proposed machine will be utilized as a mechanical transmitter for extremely/very low frequency (0.3-3 kHz) communication, which will immediately enable the bidirectional communication between the earth surface to underground or undersea facilities. The design of a UHS machine for AMEBA application presents several special challenges because it requires a high shaft torque at UHS operation. Also, the UHS machine necessitates a high design-safety-margin to avoid any catastrophic failure at the UHS operation. However, a conventional 3-phase UHS machine cannot meet the torque requirement, thermal limit, structural integrity, and fails to provide enough safety margin at UHS operation. To overcome this limitation, this paper presents the design of a high-power UHS machine, which utilizes a multi-phase winding configuration and special materials to improve the torque density and the design-safety-margin. The machine geometry and design parameters are optimized using a Multiphysics loss minimization approach. The proposed design and its performance are analyzed using extensive finite element analysis (FEA). It is observed that the proposed design meets the electromagnetic, thermal, structural, and Rotordynamic performance with a greater design-safety-margin. Finally, a prototype of the proposed machine is developed and its performances (back-EMF and natural frequencies) are experimentally validated.**

Keywords— Ultra-high-speed machine, six-phase machine, Multiphysics analysis, finite-element analysis (FEA), permanent magnet machine and mechanical-based antenna (AMEBA).

I. INTRODUCTION

Ultra-high-speed machine (UHSM) has several inherent advantages, including high efficiency, compact structure, and high-power density [1-2]. As a result, UHSM is getting more and more attention, especially in high-tech industries such as robotics, portable power, and medicine in recent years [3-6]. Apart from these, one of the promising applications of UHSM is the rapidly growing wireless communication system [7-8]. With the current technology, wireless communication in the FR-denied environment, for example, communication between the earth's surface to the underground or deep-seawater is very limited in both distance and efficiency because of the high attenuation of these conductive media. In addition, the conventional coil antenna's lower field generation efficiency causes excessive input power [9] and requires a gigantic antenna which makes portable communication impossible.

One of the most promising and power-efficient solutions to this problem is using a mechanical based-antenna (AMEBA) system which enables the possibility of under-ground and undersea communication by using extremely/very low frequency (0.3 to 10 kHz). It increases the skin depth of the electromagnetic waves that can penetrate a long distance

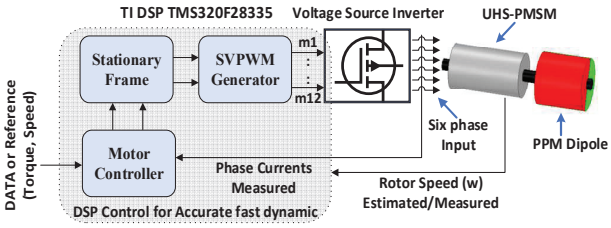

Fig. 1: Simplified diagram of a mechanically controlled antenna including UHS permanent magnet synchronous machine.

in the conductive environments [10] . A simplified diagram of the AMEBA system is shown in Fig. 1, which has four main components: a polarized permanent magnet (PPM) dipole, a UHS electrical motor, a power electronics interface, and a digital controller. Unlike a conventional electrical antenna, the mechanical antenna generates the oscillating magnetic-field using the PPM, which consumes no power. Besides, using a rear-earth magnet as a PPM improves the antenna's field generation efficiency significantly. However, one of the critical challenges in developing this AMEBA is designing its mechanical transmitter, i.e., the UHS motor to drive the PPM at the transmitting frequency up to 10 kHz. Apart from this UHS requirement, it needs a high shaft torque at the UHS operation to rotate the high mass-density rear-earth PPM. Besides, to make the complete AMEBA transmitter portable, the UHS machine should be compact, small footprint, and highly power efficient. These requirements make the design of UHSM for AMEBA application more challenging compare to the conventional high-speed machine. For example, the maximum rotational speed is limited by the rotor's high centrifugal force, the rotor' outer diameter is restricted by excessive air-friction loss in the air-gap, the critical frequencies constrain the stack length, active part's materials are influenced by the electrical losses as well as thermal limit, and the rotor assembly is constrained by manufacturing capability. Hence, it is highly recommended to design the UHSM using a Multiphysics analysis and perform a detailed investigation of its electromagnetic performance, structural integrity, thermal limit, and rotor-dynamics [11]. Otherwise, it will cause inefficient power conversion, unexpected vibration, acoustic noise, and even catastrophic failure at UHS operation.

In literature, several UHSMs are designed, having an operating speed from 200000-rpm to 1200000-rpm [12]-[15]. But, for the wide bandwidth AMEBA operation, machines having a rotational speed of 500000-rpm or more are of interest in this paper. In [16], the design of a 100-W, 500000-rpm permanent magnet synchronous motor (PMSM) was reported in 2005. Later, the same research group proposed a 100-W, 1000000-rpm PMSM using a similar design technique. A 100-W, 1200000-rpm switched reluctance machine is presented in [2], which has an unconventional

rotor geometry. These motors are designed for very low shaft torque at UHS operation: 1.9 mNm for [16] and 0.79 mNm for [2]. On the other hand, the UHSM of the AMBEA system requires a higher shaft torque at the UHS. Initially, the studied AMEBA system is aimed to transmit a 160-character message within 3 minutes in the RF-denied area using a transmitting frequency from 3 Hz to 8.3 kHz. To meet these requirements an optimal hollow cylinder (L/D = 0.73) PPM is obtained using an iterative optimization process, having inertia of $1.613 \times 10^{-4}\ kgm^2$. The total transmitter inertia is calculated as $1.658 \times 10^{-4}\ kgm^2$ and the data transition rate is considered as $\frac{12\ Hz}{0.5\ s}$. Furthermore, the 8.3 kHz transmitting frequency sets a rotational speed requirement of ~500 000 r/min for a two-pole rotor. Based on the antenna's mechanical and communication requirements, a motor is needed with a shaft torque of 32.2 mNm at 500000 rpm, resulting in a 2-kW rated power with a safety factor of 1.5. However, studies on the design of high power UHS machine (especially 2-kW, 500000-rpm) has not been done in the literature to the best of author's knowledge.

In this paper, a 2-kW, 500000-rpm UHSM is designed for AMEBA application. Instead of three-phase winding, a six-phase winding configuration is used in the proposed machine to increase the torque density. A Multiphysics parameter optimization technique is used to obtain the optimal machine parameter. The proposed machine will add a new dimension to the design of a high-power UHS machine.

II. Modeling of A 6-Phase UHS Machine

Adopting multi-phase winding configuration in a PM machine offers several inherent benefits such as high efficiency, high torque density, lower magnetomotive force harmonic, and reduced per-phase converter current rating, which makes them a suitable candidate for a UHS machine. In literature, extensive research has been done in developing multi-phase machines, especially five-phase and six-phase [17]-[18]. However, the six-phase configuration is more attractive over the five-phase one because it can be easily driven by utilizing two conventional three-phase inverters.

A six-phase winding arrangement can be classified into three main types in an electric machine based on the displacement angle, which is the phase difference between the two sets of three-phase winding. Fig. 2 shows the commonly used stator winding arrangements in a six-phase machine. A winding is called asymmetric 6-phase, symmetric 6-phase, and dual 3-phase winding when the displacement angle is 30°, 60°, and 0°. The asymmetric six-phase winding is most attractive among these three configurations because it can reduce the torque ripple by canceling the 6th torque harmonic [19]. A six-phase asymmetric winding machine is designed in [20], and its performance is compared with symmetric winding configuration. Considering the neutral point connection, a 6-phase machine stator winding has two options: single neutral point and dual neutral point. The single neutral point offers better fault-tolerant capability, but it needs extra care to control zero-sequence current. On the other hand, a dual neutral point avoids the flow of zero sequence current, making a simple PWM control and better DC bus utilization capability [21].

According to the literature, a six-phase UHSM can be mathematically modeled using two widely used control strategy: vector space decomposition (VSD) model [22] and

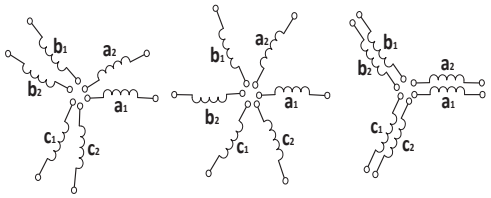

Fig. 2: Stator winding arrangement (a) Asymmetric six-phase (b) symmetric six-phase (c) Dual three-phase.

two-individual control (TIC) model [23]. VSD controls the machine as a six-phase machine. It offers a good dynamic torque performance because it does not have any mutual coupling between two winding sets. However, it has several complex matrix transformations. On the other hand, TIC treats the six-phase machine as two individual three-phase machine. Hence, it is more practical method and it can suppress the unbalance current resulting from the two asymmetric winding sets. But, TIC suffers instability issues due to the mutual magnetic coupling between two winding sets. This problem increases if the winding has stronger magnetic interaction and becomes worst at the high operating speed. Using TIC, the phase voltage and flux linkage of a six-phase PMSM can be written as:

$$V_{ABC} = R_s I_{ABC} + \frac{d(\varphi_{ABC})}{dt};\ \varphi_{ABC} = L_{ABC} I_{ABC} + \lambda_{ABC} \quad (1)$$

$$V_{DEF} = R_s I_{DEF} + \frac{d(\varphi_{DEF})}{dt};\ \varphi_{DEF} = L_{DEF} I_{DEF} + \lambda_{DEF} \quad (2)$$

where R_s is the stator phase resistance; $V_{ABC} = [V_A\ V_B\ V_C]^T$, $I_{ABC} = [I_A\ I_B\ I_C]^T$, $\varphi_{ABC} = [\varphi_A\ \varphi_B\ \varphi_C]^T$, $\lambda_{ABC} = [\lambda_A\ \lambda_B\ \lambda_C]^T$ are phase voltage vector, phase current vector, PM flux linkage vector, and airgap flux linkage vector of ABC winding set; $V_{DEF} = [V_D\ V_E\ V_F]^T$, $I_{DEF} = [I_D\ I_E\ I_F]^T$, $\varphi_{DEF} = [\varphi_D\ \varphi_E\ \varphi_F]^T$, and $\lambda_{DEF} = [\lambda_D\ \lambda_E\ \lambda_F]^T$ are the phase voltage vector, phase current vector, PM flux linkage vector, and airgap flux linkage vector of DEF winding set. L_{ABC} and L_{DEF} are inductance matrix of ABC and DEF winding set, given in (3). Using the *dq* transformation (4), the six-phase PMSM can be modeled into synchronous rotating frame as (7) to (9).

$$L_{ABC} = \begin{bmatrix} L_{aa} & L_{ab} & L_{ac} \\ L_{ba} & L_{bb} & L_{bc} \\ L_{ca} & L_{cb} & L_{cc} \end{bmatrix} \ L_{DEF} = \begin{bmatrix} L_{dd} & L_{de} & L_{df} \\ L_{ed} & L_{ee} & L_{ef} \\ L_{fd} & L_{fe} & L_{ff} \end{bmatrix} \quad (3)$$

$$V_{d_1q_10} = T_{dq01}.V_{ABC}, \text{ and } V_{d_2q_20} = T_{dq02}.V_{DEF} \quad (4)$$

T_{dq01} and T_{dq02} are transformation matrix for ABC and DEF winding set.

$$T_{dq01} = \begin{bmatrix} cos\theta & \cos(\theta - 120^0) & \cos(\theta + 120^0) \\ sin\theta & \sin(\theta - 120^0) & \sin(\theta + 120^0) \\ 0.5 & 0.5 & 0.5 \end{bmatrix} \quad (5)$$

$$T_{dq02} = \begin{bmatrix} \cos(\theta - 30^0) & \cos(\theta - 150^0) & \cos(\theta + 90^0) \\ \sin(\theta - 30^0) & \sin(\theta - 150^0) & \sin(\theta + 90^0) \\ 0.5 & 0.5 & 0.5 \end{bmatrix} \quad (6)$$

$$\begin{bmatrix} v_{d1} \\ v_{q1} \end{bmatrix} = \begin{bmatrix} R_s + sL_{d1} & -\omega L_{q1} \\ \omega L_{d1} & R_s + sL_{q1} \end{bmatrix} . \begin{bmatrix} i_{d1} \\ i_{q1} \end{bmatrix} + \omega \begin{bmatrix} 0 \\ \lambda_{PM} \end{bmatrix} \quad (7)$$

$$\begin{bmatrix} v_{d2} \\ v_{q2} \end{bmatrix} = \begin{bmatrix} R_s + sL_{d2} & -\omega L_{q2} \\ \omega L_{d2} & R_s + sL_{q2} \end{bmatrix} . \begin{bmatrix} i_{d2} \\ i_{q2} \end{bmatrix} + \omega \begin{bmatrix} 0 \\ \lambda_{PM} \end{bmatrix} \quad (8)$$

$$T_e = \frac{3}{2}.\frac{p}{2}\left[\lambda_{PM} i_{q1} + \left(L_{d1} - L_{q1}\right) i_{d1} i_{q1} + \lambda_{PM} i_{q2}\ \left(L_{d2} - L_{q2}\right)\right] \quad (9)$$

where (v_{d1}, v_{q1}), (i_{d1}, i_{q1}), and (L_{d1}, L_{q1}) are the d-q axis voltages, currents, and inductances for ABC winding, (v_{d2}, v_{q2}), (i_{d2}, i_{q2}), and (L_{d2}, L_{q2}) are the d-q axis voltages, currents, and inductances for DEF winding, ω is rotational speed (electrical), $s = \frac{d}{dt}$, p is the number of rotor poles, λ_{PM} is the PM flux linkage, and T_e is the electromagnetic torque. The proposed rotor structure has a cylindrical PM inside the sleeve, resulting $L_d = L_q$. Furthermore, the winding set ABC is identical to DEF, resulting $(L_{q1} = L_{q2} = L_q = L_{d1} = L_{d2} = L_d = L)$. Hence, T_e of the proposed UHSPMSM can be simplified as (10):

$$T_e = \frac{3}{2} \cdot \frac{p}{2} \left[\lambda_{PM} (i_{q1} + i_{q2}) \right] \quad (10)$$

The mechanical dynamics of UHS PMSM can be modeled as:

$$J \frac{d\omega}{dt} = T_e - T_L - B\omega \quad (11)$$

where J is the rotor inertia, T_L is the load torque, and B is the damping coefficient.

III. Design of the Proposed UHS Machine

In this section, the detailed design of the proposed UHS PMSM is presented, which includes the machine topology, material selection and parameter optimization.

A. Machine Topology:

In literature, different machine types have been studied for UHS operation [1]-[4]. At the required power level and speed condition, the PMSM is the best option because it has high-torque density, constant air-gap flux density, and commutation-free construction. However, the conventional PMSM topology is not suitable for a UHSM due to its excessive rotational speed. Fig. 3 shows the 2-D cross-section view of the proposed UHS PMSM topology. Unlike a conventional PMSM rotor geometry, it does not have a laminated rotor core, separated pole magnet, and steel shaft in the rotor center. Instead, a cylindrical PM is buried inside the hollow cylinder retaining sleeve and the axial extension of the sleeve forms the rotor shaft. This rotor configuration has the benefit of a sinusoidal air-gap field, smaller system volume, and high-torque density. For the stator, both slotted and slot-less configurations can be implemented [10]. In the proposed design, a slot-less configuration is considered to reduce the eddy current loss by eliminating the slot harmonics. It also has the advantage of smooth torque operation and simple manufacturing. The interference-fit installation will be used between the sleeve and PM to secure a rigid assembly of them and proper transmission of the developed torque from the magnet to the rotor shaft

B. Material Selection:

The active part's material selection for UHS PMSM has significant influences on its performance. For the stator, a high-frequency stator core material should be used to reduce the stator core loss generated by the high-frequency rotating magnetic field. Table-I shows the commonly used stator materials and their essential properties. Nanocrystalline has excellent thermal characteristics, magnetic properties, and the lowest specific loss coefficient. However, it is not readily available in the required dimension and shapes. Soft magnetic composite (SMC) and silicon iron-based materials have the highest magnetic properties with a good temperature profile,

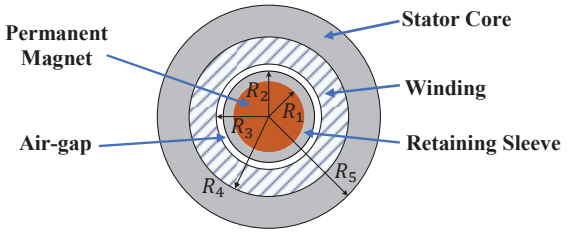

Fig. 3: 2-D cross-section of the proposed UHS machine.

Table-I: Key properties of different stator materials

Material names	Curie Temp.(°C)	Flux density (T)	Loss coefficient (W/cm3)
Nanocrystalline	528	1.32	0.02
SMC	450	2.00	2.82
Silicon-iron	700	1.75	1.88
Ferrite-iron	125	0.39	0.185
Amorphous	390	1.56	0.151

Table -II: Important properties of the PM and Sleeve material

Symbol	Quantity	SmCo (2:17)	Titanium
ρ	Density (kg/m^3)	8300	4430
E	Young's Modulus (GPa)	104	114
v	Poisson's ratio	0.28	0.35
α_{th}	Coeff. of thermal expansion $(\mu m/C)$	10	9.5
	Compressive Strength (MPa)	800	970
	Tensile Strength (MPa)	120	900

but it's used is strictly limited mainly in this high-frequency application due to the highest specific loss coefficient. Ferrite iron-based material has a lower specific loss coefficient, but it has very low saturation flux density and curie temperature. Amorphous iron-based material has a good magnetic, thermal, and electric property which makes this suitable over other materials

In the UHS operation, the stator winding has both the DC current (ohmic) and AC current (proximity) loss. At 8.33 kHz fundamental frequency, the AC losses become higher and dominating compare to DC loss. Hence, multi-strand Litz wire is used in the stator winding to reduce the high-frequency AC loss. It also offers a higher slot fill factor which reduces further copper losses by decreasing coil resistance.

The permanent magnet (PM) material should have a high remnant flux density (B_r) to ensure a high-torque density. The AMEBA rotor experiences a high working temperature due to the high air-friction loss. Considering these requirements, rear earth magnet $NdFeB$ and Sm_2Co_{17} are two candidates to use as PM. $NdFeB$ has highest B_r value, mechanically strong, and low cost, but it has an operating temperature of only 80^oC, which limits its use in the high-power UHS rotor. Hence, Sm_2Co_{17} is the only option for the studied rotor. Sm_2Co_{17} is comparatively fragile and has lower B_r, but it has high energy density (BH_{max}) at high temperature and an operating temperature up to 350^oC.

The retaining sleeve is used to provide mechanical support to the brittle PM against the developed centrifugal force during the UHS operation. Usually, a non-ferromagnetic material having high tensile strength, good thermal conductivity, and lightweight are the best choice as sleeve material. Commonly used sleeve materials are titanium alloy, stainless steel, and Inconel alloy [24]. Both the stainless steel and Inconel alloy are cheaper but have a high mass density, resulting in high centrifugal forces at the UHS rotation. In the studied rotor, titanium alloy (Ti-6Al-4V) is selected as sleeve material because it has a high elasticity

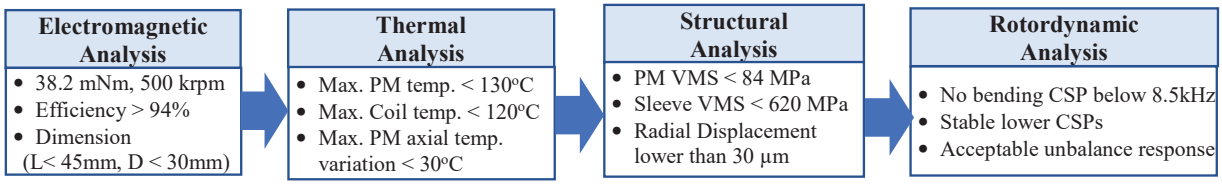

Fig. 4: Multiphysics design flow and constraints of the proposed UHS PMSM.

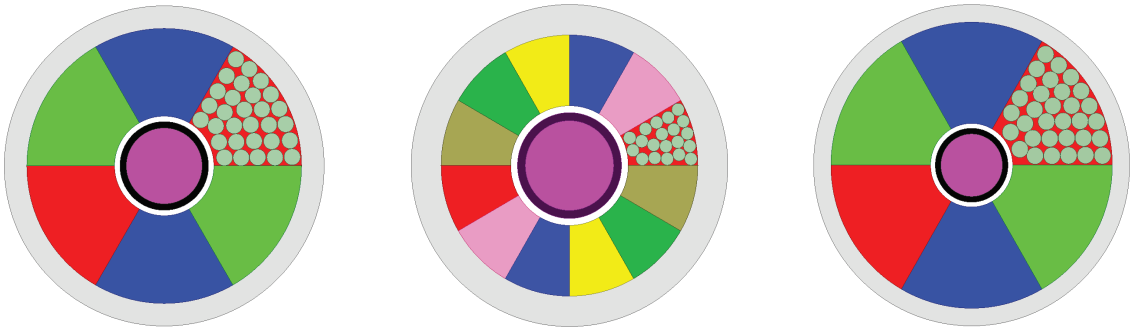

(a)
3-phase, R_1 = 4.1 mm, R_5 = 17.7
Torque = 38.2 mNm at 500 000 rpm
Efficiency = 92.5%
Air-friction loss = 85 W
Input current (rms) = 6.3 A
PM temperature = 158 ºC
VMS on PM center = 117 MPa
Stator Outer radius = 17.7 mm

(b)
6-phase, R_1 = 3.9 mm, R_5 = 14
Torque = 38.2 mNm at 500 000 rpm
Efficiency = 94.5%
Air-friction loss = 59 W
Input current (rms) = 4 A
PM temperature = 127 ºC
VMS on PM center = 84 MPa
Stator Outer radius = 14 mm

(c)
3-phase, R_1 = 3.9 mm, R_5 = 20.1
Torque = 38.2 mNm at 500 000 rpm
Efficiency = 93%
Air-friction loss = 59 W
Input current (rms) = 7.8 A
PM temperature = 135 ºC
VMS on PM center = 84 MPa
Stator Outer radius = 20.1 mm

Fig. 5: Multiphysics parameter optimization result: (a) case-I (b) case-II, (c) case-III.

modulus, lightweight, and a similar coefficient of thermal expansion of PM, ensuring a constant contact pressure at UHS operation. Table-II shows the essential properties of Sm_2Co_{17} and Ti-6Al-4V.

C. Parameter Optimization

$$S \propto R_1^2 L\omega \tag{12}$$

According to the scaling law (12) [16], the shaft output power (S) of an electric machine is proportional to its outer rotor dimensions. Hence, to increase the power rating of the UHS machine, a larger magnet radius (R_1) and extended stack length (L) are required. However, increasing R_1 and L influences the structural, thermal, and Rotordynamic limits of the UHS PMSM significantly. For example, increasing R_1 requires a thicker sleeve thickness to protect the PM from excessive centrifugal force. But, a thick sleeve increases the effective airgap length (R_4 - R_1), which decreases the torque density of the machine by reducing the electromagnetic coupling between the electric and magnetic loading. Secondly, the rotor air-friction loss is proportional to the 4th power of the outer rotor radius [8]. Hence, increasing the magnet radius increases the air-friction loss enormously, which reduces the machine efficiency abruptly. It also seriously affects the rotor temperature distribution. Thirdly, enlarging R_1 increases the required interference-fit length ($\Delta\delta_o$) exponentially, making the rotor assembly difficult. Fourthly, the magnet radial stress and sleeve stress increase proportionally with R_1.

On the other hand, increasing the rotor stack length (L) affects the AMEBA rotor's natural frequency significantly. As L increases, the value of the rotor's natural frequencies decreases, which results in several critical speed points below or near the rated speed. For AMEBA application, more critical frequencies in the rated speed region limit the antenna's communication bandwidth.

Therefore, it is concluded that the dimension (especially, R_1 and L) variation of UHS PMSM has a Multi-disciplinary influence on machine performance and design. Hence, a Multiphysics parameter optimization is used in this design to obtain the optimal design parameters. Fig. 4 shows the simplified Multiphysics workflow and its corresponding constants in different physics. An optimal design should satisfy all these Multiphysics constraints. These constraints are set based on the ABEAM application requirements.

This Multiphysics optimization is a highly iterative process. Both the analytical model and FEA model are used in this optimization. The model can be optimized for different objective functions such as weight, torque, loss, cost, and volume. A loss minimization objective function is considered in the design.

In this paper, three different cases are studied using different optimization scenarios to justify the proposed design. Similar design techniques, materials, and loss minimizing optimization are used in all cases. Also, the stack length (40 mm), strand diameter (0.078 mm), sleeve thickness (0.7 mm), air-gap (0.6 mm), air-cooling system (current density < 5 A/mm^2), and rated power (2-kW) are kept constant. A summary of the optimization result is presented in Fig. 5.

In case-I, an attempt is taken to design the required machine using a conventional three-phase winding. In this case, no optimal design is found when all Multiphysics constraints are applied. It is observed that the optimized solution does not meet the required electromagnetic performance when the structural and thermal limits are considered. However, when the thermal and structural limits are ignored, the design meets the desired electromagnetic

performance, shown in Fig. 5(a). In this design, the optimal R_1 is obtained as 4.1 mm to produce the required torque (38.2 mNm). However, it causes a high air-friction loss (85 W) on the rotor surface, resulting in a PM temperature of 158° C. It also generates a high centrifugal force on the PM, resulting a VMS of 117 MPa on the PM center at 500 000 rpm. Both the PM temperature and stress value exceed the allowable limit. Each phase has 30 turns and an input current of 6.3 A (RMS). To supply this current, a Litz wire of 150 strands is required, which makes the coil diameter 1.72 mm, including the insulation. Though this design meets the electromagnetic torque requirements, its efficiency is only 92.5%, and it exceeds the outer stator radius limit. However, it should mention that if the structural stress and thermal limit are not satisfied, a UHSM will experience severe NVH issues leading to catastrophic failure while operating UHS condition.

In case-II, the machine is optimized using a six-phase winding configuration, and all Multiphysics constraints are applied. The optimized design and its key performances are shown in Fig. 5(b). Adopting a six-phase winding increases the stator's electric loading density. This inherent benefit of multiphase winding allows the machine to use a lower magnetic loading. Hence, the magnet radius is decreased to 3.9 mm in the optimized design which limits the centrifugal stress (at 500000 rpm) on PM to 84 MPa only. It also reduces the air-friction loss by 30% of case-1, resulting in the maximum PM temperature below 130°C. Another advantage of Multiphase winding configuration is it minimizes the per-phase current (or power) rating. Using this benefit, the optimal design minimizes the input RMS current to 4 A only, which reduces the copper loss by 19% of case-1. As the input current decreased by 37%, a Litz wire of 100 strands is used, which has a diameter of 1.12 mm only. It has 20 turns per-phase which makes the stator outer diameter within the acceptable limit. Therefore, it is concluded that this design is optimal and it satisfies all the Multiphysics constraints.

In case-III, the machine is again optimized using three-phase winding, but this time the magnet radius (R_1) is kept constant at 3.9 mm. The optimization result is shown in Fig 5(c). Similar to case-II the design limits the PM stress to 84 MPa and the air-friction loss to 60 W. However, the stator draws a 7.8 A (RMS) input current to develop the required torque, which is two times that of the optimal design (case-II). This high input current increases the winding's copper loss to 76 W, which decreases the machine efficiency and increases the winding temperature. As the input current increase, the number of required strands also increases to 185, making the coil diameter 2.02 mm. As a result, the design requires an outer stator radius of 20.1 mm, which is 50 % high than the maximum available limit. Therefore, though this design satisfies the electromagnetic torque and structural limit, it does not meet the dimension constraints, thermal limit, and efficiency constraint.

IV. Simulation Results and Analysis

In this section, the performance of the optimized 2-kW UHS PMSM is analyzed using extensive FEA simulation. The optimal design parameters are $R_1 = 3.9$ mm, $R_2 = 4.6$ mm, $R_3 = 5.2$ mm, $R_4 = 11.25$ mm, $R_5 = 14$ mm, $\Delta\delta_o = 20$ µm, and $L = 40$ mm.

A. Electromagnetic Analysis:

In the proposed UHS PMSM, the Litz wire can be implemented as either toroidal winding or self-supported cup-shaped surface winding. Since the studied machine is prototyped in the lab, a toroidal winding is considered to ease the manufacturing process. A six-phase asymmetric winding configuration with a displacement angle of 30° is implemented in the proposed design, as shown in Fig. 2 (a). Each phase coil has 40 turns in series, and two neutral points are separated. The six-phase back-EMF and input current profile at 500000 rpm are shown in Fig. 6(a) and Fig. 6(b). The B-EMF is pure sinusoidal due to the ring shape rotor and slot-less stator; it has a desire peak value of 124 V.A sinusoidal input current of 5.65 peak is required to generate the rated electromagnetic torque. Fig. 6(c) shows the developed electromagnetic torque which has an average desire value of 38.2 Nm at 500000 rpm to provide 2000 W rated power. It also shows the torque generated by an input current having 5% of 5th harmonics, 3% of 8th harmonics, and 1% of 11th harmonics. These harmonics are added in the input current intentionally to check the torque profile in non-ideal cases. Fig. 6(d) shows the phase to neutral flux linkage generated at 500000 rpm with no current. It has a peak value of 0.024 Wb. The magnetic flux density at rated current condition is shown in Fig. 7, and the maximum flux density is 0.61 Wb.

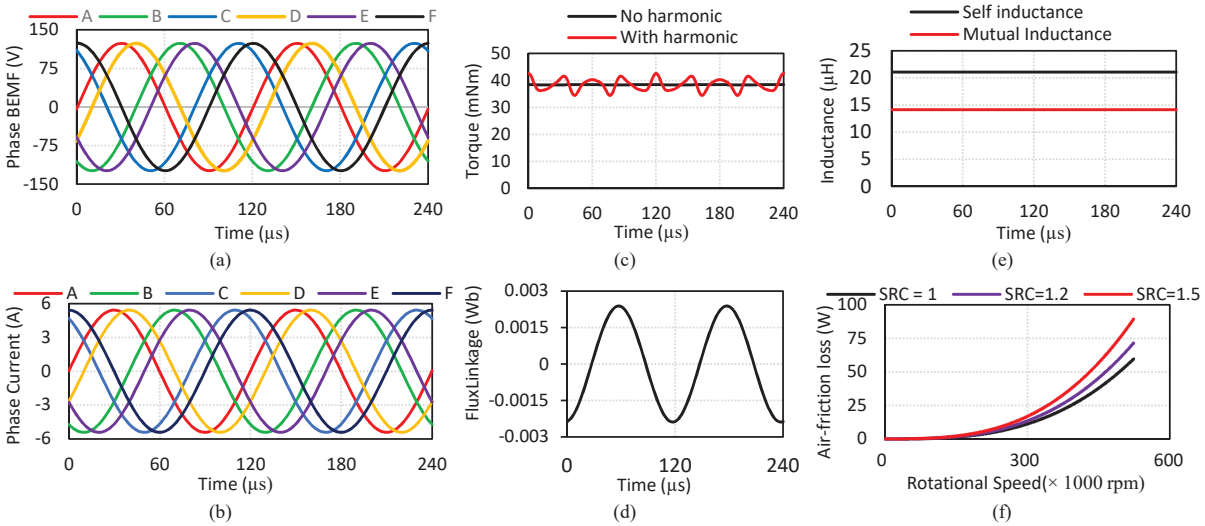

Fig. 6: (a) B-EMF, (b) input current, (c) electromagntic torque, (d) flux linkage, (e) stator core loss (f) air-friction loss of the proposed UHS PMSM

The mutual interaction (MI) between the two sets of three-phase winding can be calculated using FEA simulation. A DC current is supplied to ABC winding set (I_a = 1A, I_b = -0.5A, I_c = -0.5A) and DEF winding set is disconnected. Both the sleeve and PM are removed to ensure zero flux density in the rotor. The MI is calculated by means of the ratio between the mutual inductance and self-inductance. Fig. 6(e) shows the mutual interaction in the proposed UHSPMSM is 67%. This is rational because the ABC winding set shares the slot of DEF winding.

The stator core loss is investigated using three materials: ferrite iron (Epcos-N87), silicon iron (50PN595), and amorphous iron (Metglas-2605SA1). As shown in Fig. 8, the maximum stator core loss is 34 W at rated speed, which occurs in the 50PN595. Though N87 has the lowest core loss, it is not suitable to use as a stator core because the magnetic flux density in the stator core exceeds the saturation level of N87, which is 3.9 T. Hence, the amorphous Metglas is considered as stator core which has a core loss of 2.2 W at 500000 rpm. Fig. 6(f) shows the air-friction loss versus rotational speed at different surface roughness coefficient (SRC). It is 60 W at 500000 rpm considering a unity SRC. The total copper loss at 500000 rpm is calculated 48 W, where the AC proximity loss is 36 W, and DC ohmic loss is 12 W. The magnet eddy current loss is only 0.2 W because the titanium alloy has a very-low loss coefficient and the stator current is sinusoidal. The proposed model has 97.5% electrical efficiency and total efficiency of 94.5%, considering both electrical and windage loss. Compare to the 3-phase model, the proposed model improves the overall efficiency from 92.5% to 94.5%.

B. Thermal Analysis:

3-D FEA model is used to analyze the temperature distribution of the proposed UHSPMSM. Two-way coupling between electromagnetic solver and thermal solver is used for this study. Different losses (copper loss, stator core loss, rotor eddy current loss, air-friction loss) obtained from the electromagnetic solver are imported as a load to the thermal model's corresponding materials. The boundary condition is applied according to the actual motor cooling system. The natural air-cooling system is considered in the prototype with an ambient temperature of 25°C. Fig. 9 shows the temperature distribution of the machine at rated condition. The maximum temperature is 127°C, which occurred in the PM. The air-friction loss is the dominant factor of this temperature. The winding temperature is 102°C, and the stator core temperature is 82°C. All these temperature values are within the desired limit. It is also observed that the temperature distribution on the rotor and PM is not linear, rather it increases gradually from the edge to the center of the magnet and follows an axial axis symmetry.

C. Structural Analysis:

Fig. 10 presents the von-mises equivalent stress (VMES) distribution on the proposed rotor at a standstill and rated speed conditions. The temperature effect is also included to consider the thermal expansion. At a standstill, the PM experiences compressive stress of 82 MPa, and the sleeve experiences a VMES of 538 MPa at the contact zone due to the implementation of interference fit. At 500000 rpm, PM's compressive force becomes radial stress, which generates a VMES of 83 MPa at the PM center. At 500000 rpm, the sleeve inner edge experiences the maximum VMES

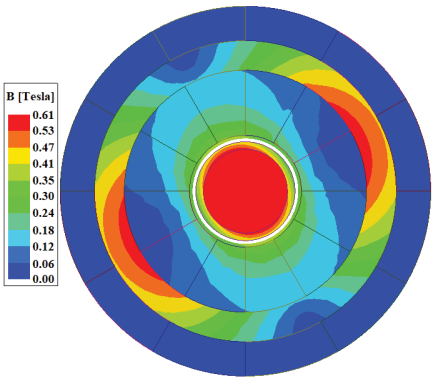

Fig. 7: Flux density of the UHS PMSM at rated condition.

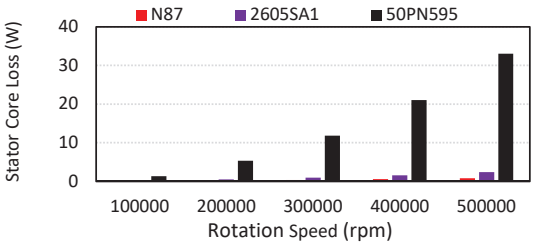

Fig. 8: Stator core loss at different material and rotational speed.

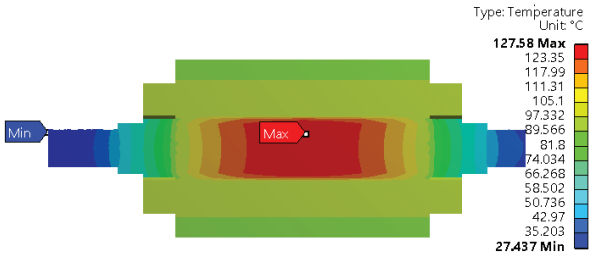

Fig. 9. Temperature distribution at rated condition.

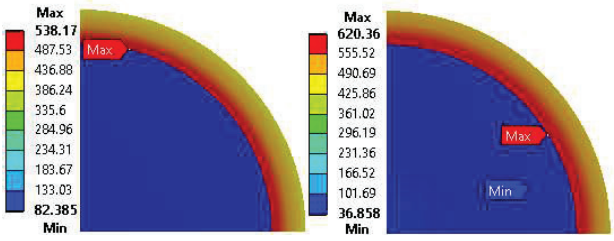

Fig. 10: Structural analysis FEA result: (left) standstill at ambient temperature 25 °C, (Right) 500 000 r/min at working temperature 130 °C.

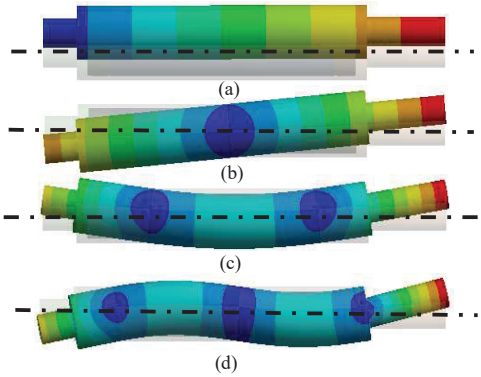

Fig. 11: (a) Lateral mode (95 Hz), (b) Conical mode (195 Hz), (c) 1st order bending mode (9012 Hz), and (d) 2nd order bending mode (17053 Hz)

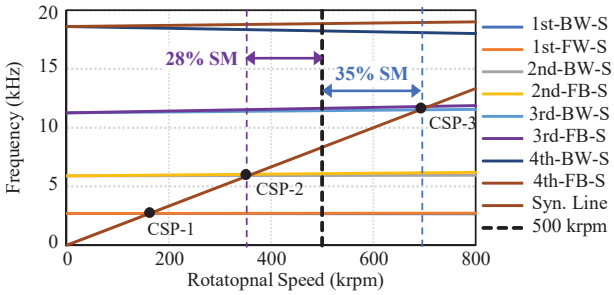

Fig. 12: Campbell diagram of the UHS AMEBA rotor.
[S-stable, US-unstable, CSP- critical speed point]

of 620 MPa. Hence, the proposed model offers a 30% structural safety margin to the rotor material at the maximum operating speed.

D. Rotordynamic Analysis

The natural frequency of the proposed rotor is analyzed by the modal simulation using Ansys FEA. First, modal simulation is carried out under free-free boundary conditions to observed the undamped natural frequencies and their mode shape. According to the simulation result, the first four natural frequencies are 95 Hz, 195 Hz, 9012 Hz, 17053 Hz. The first two lower frequencies are rigid body frequency, generating a lateral (95 Hz) mode shape and a conical (195 Hz) mode shape. Furthermore, the third and fourth frequencies generate the 1st (9012 Hz) and 2nd (17053 Hz) order bending mode shape. Fig. 11 shows the AMEBA rotor's deformation modes at these frequencies. Then the variation of the first four natural frequencies with different bearing stiffness values are analyzed and based on the result, the suitable bearing stiffness is selected. In a UHSM, the selection of bearing is critical, and it depends on various factors. In literature, researchers have studied different bearings for UHS operation. However, the Ball bearing is the first choice for an electric machine because of its simplest design and high robustness, high stiffness value, though it has a high friction loss and limited lifetime. In this study, the ball bearing is used, which has a stiffness value of 10.1 M N/m. The natural frequencies are also observed after applying the selected bearing. Fig. 12 shows the studied rotor's Campbell diagram. It is observed that Due to the guide bearing stiffness, the rigid body modes are moved from 95 Hz to 2806 Hz and 195 Hz to 5956 Hz. The first bending frequency is shifted from 9098 Hz to 11250 Hz, and the second bending is also shifted from 17015 Hz to 21003 Hz. Consequently, the rated speed point falls between the 2nd and 3rd critical speed points. However, there is a 28% separation margin (SM) between the 2nd critical speed point and rated speed; and 35% SM considering the 3rd critical speed point.

V. Prototype and Experimental Validation

Fig. 13 shows the different parts and the assembly of the proposed machine. The titanium sleeve and shaft parts are designed using CNC machining technology. A pair of customized UHS ball bearing is used, which can operate at 500000 rpm continuously for 15 hours. The calendarial PM (Sm_2Co_{17}) is diametrically magnetized. A 6-phase asymmetric toroidal winding is applied on the Metglas-2605SA1 stator core. Each phase winding has 40 turns in series and each turn has 100 strands of 40-AWG copper Litz wire. The interference-fit between the magnet and sleeve is

The insulated slot-less stator core

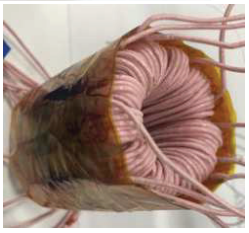

6-phase toroidal winding

Fig. 13: UHS AMEBA rotor parts and assembly.

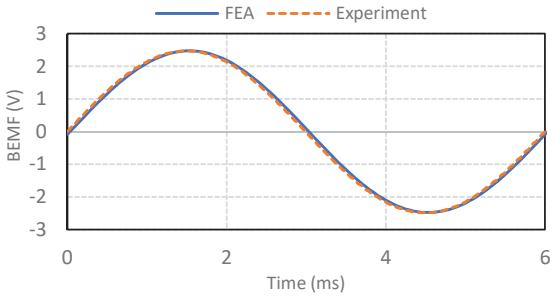

Fig. 14: No load B-EMF of phase-A at 10000 rpm.

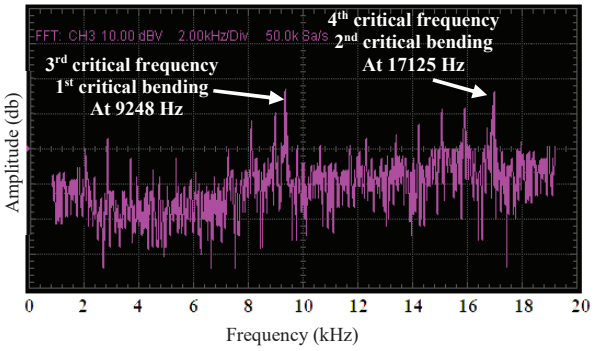

Fig. 15 Frequency spectrum of impulse hammer test.

implemented using the shrink-fit technique, where liquid nitrogen (LN) is used to cool down the magnet, and an induction heater is used to heat the sleeve. An interference flit of 20 µm is applied between them.

Initially, the B-EMF of the proposed machine is measured at 10000 rpm. Fig. 14 shows the six-phase B-EMF generated by both simulation and experimental analysis. The experimental result shows a B-EMF constant of 2.5 $\times 10^{-4}$ V/rpm, which is closely matched with the simulation result.

An impulse hammer testing is performed to validate the proposed rotor's natural frequencies obtained by FEA simulation. A tip changeable impulse hammer is used to

excite the rotor mechanically, and an IEPE acceleration sensor is used to measure the rotor's frequency response. Fig. 15 shows the frequency response function (FRF) of the assembled AMEBA rotor when a mechanical excitation is applied using an impulse hammer. The plot is obtained by performing FFT of the acceleration sensor's output signal. In the plot, the first two rigid body modes are not separable due to their low amplitude. However, two separable peaks are visible in the spectrum at 9248 Hz and 17125 Hz, confirming the first and second bending modes. The experimental results have an excellent agreement with the simulation results with an error of 1.6%, which is acceptable because a complete free-free boundary condition is not possible in practice.

VI. Conclusion

This paper presents the modeling and design of a 2-kW and 500000-rpm UHS PMSM for AMEBA application. At first, the modeling of a 6-phase machine is presented by addressing different issues such as displacement angle selection, neutral point selection, and six-phase control theory. Then, the proposed model's design process is discussed, including machine topology, material selection, and parameter optimization. A Multiphysics loss optimization algorithm is used to obtain the optimal machine parameters. It has been observed that a design with 3-phase conventional winding does not meet the desire requirements, especially the torque, structural, and thermal requirements. Hence, a six-phase winding configuration is adopted in the proposed motor to increase the torque density. Also, special high-frequency materials are used to improve machine efficiency and Multiphysics performance. A low loss coefficient amorphous core is used as slot-less stator material. Litz wire is used to reduce high-frequency loss in the copper winding. The rotor is developed using high-strength titanium alloy. Then the performance of the proposed machine is analyzed using extensive FEA simulation. FEA results show that the proposed model satisfies all the Multiphysics requirements and improves efficiency from 92.5% to 94.5%. A prototype of the proposed UHSPMSM is built. Initially, the no-load B-EMF is measured at 10000 rpm, which closely matched the simulation result. An experiment of impulse hammer testing is performed to validate the FEA modal analysis of the proposed design. The experiment results confirm the 1st and 2nd critical bending frequencies with an error of 1.6%.

Acknowledgment

This research was supported in part by the National Science Foundation CCSS-Comms Circuits &Sens System Program (Award Number 1905434).

References

[1] J. Dang, S. Haghbin, Y. Du, C. Bednar, H. Liles, J. Restrepo*, et al.*, "Electromagnetic design considerations for a 50,000 rpm 1kW Switched Reluctance Machine using a flux bridge," in *Electric Machines & Drives Conference (IEMDC), 2013 IEEE International*, 2013, pp. 325-331.

[2] C. Gong and T. Habetler, "A novel rotor design for ultra-high speed switched reluctance machines over 1 million rpm," in *2017 IEEEInternational Electric Machines and Drives Conference (IEMDC)*, 2017, pp. 1-6.

[3] K. Isomura *et al.*, "Experimental verification of the feasibility of a 100Wclass micro-scale Gas turbine at an impeller diameter of 10 mm," *J. Micromech. Microeng.*, vol. 16, no. 9, pp. 254–261, Mar. 2006.

[4] C. H. Park, S. K. Choi, and S. Y. Ham, "Design and experiment of 400,000 rpm high speed rotor and bearings for 500W class micro gas turbine generator," in *Proc. Int. Conf. Micro Nanotechnol. Power Gener.Energy Convers. Appl.*, Daejeon, 2011, pp. 1–4.

[5] A. Borisavljevic, *Limits, Modeling and Design of High-Speed Permanent Magnet Machines*, Zutphen, The Netherlands: Wormann Print Service, 2011.

[6] D. Kr¨ahenb¨uhl, C. Zwyssig, H. Weser, and J. W. Kolar, "A miniature 500000-r/min electrically driven turbocompressor," *IEEE Trans. Ind. Appl.*, vol. 46, no. 6, pp. 2459–2466, Nov. 2010.

[7] M. T. B. Tarek, S. Dharmasena, A. Madanayake, S. Choi, J. Glickstein, J. Liang, and S. Mandal, ''Power-efficient data modulation for allmechanical ULF/VLF transmitters,'' in Proc. IEEE 61st Int. Midwest Symp. Circuits Syst. (MWSCAS), Aug. 2018, pp. 759–762.

[8] A. Madanayake, S. Choi, M. Tarek, S. Dharmasena, S. Mandal, J.Glickstein,andA.Sehirlioglu,''Energy-efficientULF/VLFtransmitters based on mechanically-rotating dipoles,'' in Proc. Moratuwa Eng. Res. Conf. (MERCon), May 2017, pp. 230–235.

[9] S. Gong, Y. Liu, and Y. Liu, "A Rotating-Magnet Based Mechanical Antenna (RMBMA) for ELF-ULF Wireless Communication," *Progress In Electromagnetics Research M*, Vol. 72, 125-133, 2018.

[10] J. S. Glickstein, J. Liang, S. Choi, A. Madanayake and S. Mandal, "Power-Efficient ELF Wireless Communications Using Electro-Mechanical Transmitters," in IEEE Access,vol. 8, pp. 2455-2471, 2020

[11] N. Uzhegov, E. Kurvinen, J. Nerg, J. Pyrhönen, J. T. Sopanen and S. Shirinskii, "Multidisciplinary Design Process of a 6-Slot 2-Pole High-Speed Permanent Magnet Synchronous Machine,"in IEEE Transactions on Industrial Electronics,vol.63,no.2,pp.784-795,Feb. 2016

[12] D. Zhao, B. Blunier, F. Gao, M. Dou and A. Miraoui, "Control of an Ultrahigh-Speed Centrifugal Compressor for the Air Management of Fuel Cell Systems," in IEEE Transactions on Industry Applications, vol. 50, no. 3, pp. 2225-2234, May-June 2014.

[13] C. Bi, "HDD spindle motor system design for data recording with ultrahigh TPI," 2009 Asia-Pacific Magnetic Recording Conference, Singapore, 2009, pp. 1-2.

[14] D. Jung, J. Lee, J. Kim, I. S. Jang, J. Lee and H. Lee, "Design Method of an Ultrahigh Speed PM Motor/Generator for Electric-Turbo Compounding System," in IEEE Transactions on Applied Superconductivity, vol. 28, no. 3, pp. 1-4, April 2018, Art no. 5202804,

[15] C. Zwyssig, J. W. Kolar, and S. D. Round, "Megaspeed drive systems: Pushing beyond 1 million r/min," *IEEE/ASME Transactions on mechatronics,* vol. 14, pp. 564-574, 2009.

[16] C. Zwyssig, J. Kolar, W. Thaler and M. Vohrer, "Design of a 100 W 500000 rpm permanent-magnet generator for mesoscale gas turbines", *Fourtieth IAS Annual Meeting. Conference Record of the 2005 Industry Applications Conference 2005*, pp. 253-260, 2005.

[17] J. K. Pandit, M. V. Aware, R. V. Nemade and E. Levi, "Direct Torque Control Scheme for a Six-Phase Induction Motor With Reduced Torque Ripple," in IEEE Transactions on Power Electronics, vol. 32, no. 9, pp. 7118-7129, Sept. 2017, doi: 10.1109/TPEL.2016.2624149.

[18] M. K. Islam and S. Choi, "Analysis of Axial Temperature Variation Effect on the Performance of Five-Phase Permanent Magnet assisted Synchronous Reluctance Motor," 2020 IEEE Energy Conversion Congress and Exposition (ECCE), Detroit, MI, USA, 2020, pp. 1107-1114,

[19] R. H. Nelson and P. C. Krause, "Induction Machine Analysis for Arbitrary Displacement Between Multiple Winding Sets," IEEE Trans. Power Appar. Syst., vol. PAS-93, no. 3, pp. 841–848, 1974.

[20] H. S. Che and W. P. Hew, "Dual three-phase operation of single neutral symmetrical six-phase machine for improved performance," IECON 2015 - 41st Annual Conference of the IEEE Industrial Electronics Society, Yokohama, 2015, pp. 001176-001181,

[21] Y. Hu, Z. Q. Zhu and M. Odavic, "Comparison of Two-Individual Current Control and Vector Space Decomposition Control for Dual Three-Phase PMSM," in IEEE Transactions on Industry Applications, vol. 53, no. 5, pp. 4483-4492, Sept.-Oct. 2017,

[22] Y. Zhao and T. A. Lipo, "Space vector PWM control of dual three-phase induction machine using vector space decomposition," IEEE Trans. Ind. Appl., vol. 31, no. 5, pp. 1100–1109, Sep./Oct. 1995.

[23] R. Bojoi, M. Lazzari, F. Profumo, and A. Tenconi, "Digital field-oriented control for dual three-phase induction motor drives," IEEE Trans. Ind. Appl., vol. 39, no. 3, pp. 752–760, May/Jun. 2003.

[24] F. R. Ismagilov, N. Uzhegov, V. E. Vavilov, V. I. Bekuzin and V. V. Ayguzina, "Multidisciplinary Design of Ultra-High-Speed Electrical Machines," in IEEE Transactions on Energy Conversion, vol. 33, no. 3, pp. 1203-1212, Sept. 2018.